PROCEEDINGS, 44th Workshop on Geothermal Reservoir Engineering
Stanford University, Stanford, California, February 11-13, 2019
SGP-TR-214

Code Modifications for Modeling Chemical Tracers and Embedded Natural Fractures at EGS Collab

Philip Winterfeld[1], Bud Johnston[2], Koenraad Beckers[3], Yu-Shu Wu[1], and the EGS Collab Team[4]

[1]Petroleum Engineering Department, Colorado School of Mines, Golden, CO 80401

[2]Geothermal Technologies Program, National Renewable Energy Laboratory, Golden, CO 80401

[3]Heateon, Gent, Belgium

Email: pwinterf@mines.edu

Keywords: Enhanced geothermal systems, EGS Collab, Sanford Underground Research Facility, reservoir simulation, tracers, natural fractures

ABSTRACT

The EGS Collab SIGMA-V project is a multi-lab and university collaborative research project that is being undertaken at the Sanford Underground Research Facility (SURF) in South Dakota. The project consists of studying stimulation, fluid-flow, and heat transfer processes at a scale of 10-20 m, which is readily amenable to detailed characterization and monitoring. One objective of the project is to establish circulation from injector to producer by hydraulically fracturing the injector.

Data generated during these experiments is to be compared with predictions from coupled thermal, hydrological, mechanical, and chemical simulators. One such a simulator, TOUGH2-CSM, has been enhanced in order to simulate EGS Collab SIGMA-V project experiments. These modifications include adding tracers, the capability to model tracer sorption, and an embedded fracture formulation.

A set of example problems validate our conservative tracer transport and sorption formulations. We then simulated tracer transport and thermal breakthrough for the first EGS Collab SIGMA-V experiment.

1. INTRODUCTION

The EGS Collab SIGMA-V project is a multi-lab and university collaborative research project that is concerned with intermediate-scale EGS reservoir creation processes. The project site was chosen to be the Sanford Underground Research Facility (SURF) in South Dakota, a mined underground research laboratory. The project consists of studying stimulation, fluid-flow, and heat transfer processes at a scale of 10-20 m, which is readily amenable to detailed characterization and monitoring. At SURF, there are 8 boreholes drilled in metamorphic rock at 4850 ft depth. Six of the boreholes are for monitoring the experiments, one borehole is for fluid injection, and one is for fluid production. The sub-horizontal injector and producer are spaced about 10 m apart. One objective of the project is to establish circulation from injector to producer by hydraulically fracturing the injector. There are natural fractures between these two wells and once adequate circulation is established, fracture surface areas and flow pathways are to be characterized using various tracers.

The first experiment out of three proposed consists of multiple stimulations and is accompanied by comprehensive geophysical, hydrological, and geomechanical monitoring and interwell flow tests with tracers for geophysical, hydrological, geomechanical, and thermal characterization of the resulting stimulated network.

Data generated during these experiments is to be compared with predictions from coupled thermal, hydrological, mechanical, and chemical simulators. One such a simulator is TOUGH2-CSM (Winterfeld and Wu, 2014). TOUGH2-CSM is based on the TOUGH2-MP general multiphase, multicomponent, and multiporosity fluid and heat transport formulation and utilizes TOUGH2 fluid property calculation modules. The simulator geomechanical formulation is based on an equation that calculates mean stress as well as those that calculate individual stress tensor components. In addition, permeability and porosity can depend on the stress tensor and other variables. TOUGH2-CSM has been applied to simulating carbon dioxide sequestration and geothermal reservoir engineering. In this

[4] J. Ajo-Franklin, S.J. Bauer, T. Baumgartner, K. Beckers, D. Blankenship, A. Bonneville, L. Boyd, S. Brown, S.T. Brown, J.A. Burghardt, T. Chen, Y. Chen, K. Condon, P.J. Cook, D. Crandall, P.F. Dobson, T. Doe, C.A. Doughty, D. Elsworth, J. Feldman, A. Foris, L.P. Frash, Z. Frone, P. Fu, K. Gao, A. Ghassemi, H. Gudmundsdottir, Y. Guglielmi, G. Guthrie, B. Haimson, A. Hawkins, J. Heise, M. Horn, R.N. Horne, J. Horner, M. Hu, H. Huang, L. Huang, K.J. Im, M. Ingraham, R.S. Jayne, T.C. Johnson, B. Johnston, S. Karra, K. Kim, D.K. King, T. Kneafsey, H. Knox, J. Knox, D. Kumar, K. Kutun, M. Lee, K. Li, R. Lopez, M. Maceira, P. Mackey, N. Makedonska, C.J. Marone, E. Mattson, M.W. McClure, J. McLennan, T. McLing, C. Medler, R.J. Mellors, E. Metcalfe, J. Miskimins, J. Moore, J.P. Morris, S. Nakagawa, G. Neupane, G. Newman, A. Nieto, C.M. Oldenburg, W. Pan, T. Paronish, R. Pawar, P. Petrov, B. Pietzyk, R. Podgorney, Y. Polsky, J. Popejoy S. Porse, B.Q. Roberts, M. Robertson, W. Roggenthen, J. Rutqvist, D. Rynders, H. Santos-Villalobos, M. Schoenball, P. Schwering, V. Sesetty, C.S. Sherman, A. Singh, M.M. Smith, H. Sone, F.A. Soom, C.E. Strickland, J. Su, D. Templeton, J.N. Thomle, C. Ulrich, N. Uzunlar, A. Vachaparampil, C.A. Valladao, W. Vandermeer, G. Vandine, D. Vardiman, V.R. Vermeul, J.L. Wagoner, H.F. Wang, J. Weers, J. White, M.D. White, P. Winterfeld, T. Wood, S. Workman, H. Wu, Y.S. Wu, Y. Wu, E.C. Yildirim, Y. Zhang, Y.Q. Zhang, J. Zhou, Q. Zhou, M.D. Zoback

paper, we describe enhancements made to TOUGH2-CSM in order to apply it to simulate EGS Collab SIGMA-V project experiments. These modifications include adding tracers to a TOUGH2 property module, the capability to model tracer sorption, and an embedded fracture formulation. In addition, we present example problems to illustrate the performance of our enhancements as well as some results from our simulation of the ongoing first EGS Collab SIGMA-V project experiment.

2. TOUGH2-CSM FORMULATION

The TOUGH2-CSM fluid and heat flow formulation is based on the TOUGH2 formulation (Pruess *et al.*, 1999) of mass and energy conservation equations that govern fluid and heat flow in general multiphase, multicomponent, multi-porosity systems. The conservation equations for mass and energy can be written in differential form as:

$$\frac{\partial M^k}{\partial t} = \nabla \cdot \bar{F}^k + q^k \tag{1}$$

where M^k is conserved quantity k per unit volume, q^k is source or sink per unit volume, and $\bar{F}^k$ is flux. Mass per unit volume is a sum over phases:

$$M^k = \phi \sum_l S_l \rho_l X_l^k \tag{2}$$

where ϕ is porosity, subscript l denotes a phase, S is phase saturation, ρ is mass density, and X is mass fraction of component k. Energy per unit volume accounts for internal energy in rock and fluid and is the following:

$$M^{N+1} = (1-\phi) C_r \rho_r T + \phi \sum_l S_l \rho_l U \tag{3}$$

where ρ_r is rock density, C_r is rock specific heat, T is temperature, U is phase specific internal energy, and N is the number of mass components with energy as conserved species N+1.

Fluid advection is described with a multiphase extension of Darcy's law; in addition, there is diffusive mass transport in all phases. Advective mass flux is a sum over phases:

$$\bar{F}_{adv}^k = \sum_l \bar{F}_l X_l^k \tag{4}$$

and phase flux, $\bar{F}_l$, is given by Darcy's law:

$$\bar{F}_l = -k \frac{k_{rl}\rho_l}{\mu_l} \left(\nabla P + \nabla P_{c,l} - \rho_l \bar{g} \right) \tag{5}$$

where k is absolute permeability, k_r is phase relative permeability, μ is phase viscosity, P is pore pressure, P_c is phase capillary pressure, and $\bar{g}$ is gravitational acceleration. The pressure in phase l:

$$P_l = P + P_{c,l} \tag{6}$$

is relative to a reference phase, which is the gaseous phase. Diffusive mass flux is contained in the expression:

$$\bar{F}_{dis}^k = \sum_l \rho_l \bar{\bar{D}}_l^k \nabla X_l^k \tag{7}$$

where $\bar{\bar{D}}_l^k$ is the dispersion tensor. Heat flux occurs by conduction and convection, the latter including sensible as well as latent heat effects, and includes conductive and convective components:

$$\bar{F}^{N+1} = -\lambda \Delta T + \sum_l h_l \bar{F}_l \tag{8}$$

where λ is thermal conductivity and h_l is phase l specific enthalpy.

The description of thermodynamic conditions is based on the assumption of local equilibrium of all phases. Fluid and formation parameters can be arbitrary nonlinear functions of the primary thermodynamic variables.

The TOUGH2-CSM geomechanical formulation (Winterfeld and Wu, 2015) is based on the linear theory of elasticity applied to multi-porosity, non-isothermal (thermo-multi-poroelastic) media. The first two fundamental relations in this theory are the relation between the strain tensor and the displacement vector, u:

$$\bar{\bar{\epsilon}} = \frac{1}{2} \left(\nabla \bar{u} + \nabla \bar{u}^t \right) \tag{9}$$

and the static equilibrium equation, which is an expression of momentum conservation:

$$\nabla \cdot \bar{\bar{\tau}} + \bar{F}_b = 0 \tag{10}$$

where $\bar{F}_b$ is the body force.

The last fundamental relation in this theory is the relation between the stress and strain tensors, Hooke's law for a thermo-multi-poroelastic material (Winterfeld and Wu, 2014):

$$\bar{\bar{\tau}} - h(\bar{P},\bar{T}) = \lambda \epsilon_v + 2G\bar{\bar{\epsilon}} \tag{11}$$

$$h(\bar{P},\bar{T}) = \sum_j \left(\alpha_j P_j + 3\beta K \omega_j (T_j - T_{ref})\right) \tag{12}$$

where the subscript j refers to a porous continuum, ω is the porous continuum volume fraction, G is shear modulus, and λ is the Lamé parameter, α is Biot's coefficient, T_{ref} is reference temperature for a thermally unstrained state, K is bulk modulus, and β is linear thermal expansion coefficient.

We substitute Equations 9 and Equation 11 into Equation 10 and assume rock properties are constant to obtain the thermo-multi-poroelastic version of the Navier equation:

$$(\lambda + \mathrm{G})\nabla\epsilon_v + G\nabla^2\bar{u} + \nabla h(\bar{P},\bar{T}) + \bar{F}_b = 0 \tag{13}$$

We take the trace of Equation 11 and obtain a relation between mean stress, volumetric strain, pore pressures, and temperatures:

$$K\epsilon_v = \tau_m - h(\bar{P},\bar{T}) \tag{14}$$

Finally, we take the divergence of Equation 13 and utilize Equation 11 and Equation 14 to obtain an equation relating mean stress, pore pressures, temperatures, and body force - the Mean Stress equation:

$$\frac{3(1-\nu)}{1+\nu}\nabla^2\tau_m - \frac{2(1-2\nu)}{1+\nu}\nabla^2 h(\bar{P},\bar{T}) + \nabla \cdot \bar{F}_b = 0 \tag{15}$$

Equation 13 is a vector equation and each component along with its derivatives are zero. We obtain stress tensor component equations from those derivatives, for example the x-derivative of the x-component yields an equation containing the xx-normal stress component, mean stress, pore pressures, and temperatures:

$$\frac{2\nu-1}{2(1+\nu)}\frac{\partial^2 h(\bar{P},\bar{T})}{\partial x^2} + \frac{3}{2(1+\nu)}\frac{\partial^2\tau_m}{\partial x^2} + \frac{1}{2}\nabla^2\left[\tau_{xx} - \frac{3\nu}{1+\nu}\tau_m + \frac{2\nu-1}{1+\nu}h(\bar{P},\bar{T})\right] + \frac{\partial F_{b,x}}{\partial x} = 0 \tag{16}$$

In addition, differentiating the x-component of Equation 13 by y, the y-component of Equation 13 by x, and averaging the two yields an equation containing the xy-shear stress component, mean stress, pore pressures, and temperatures:

$$\frac{2\nu-1}{2(1+\nu)}\frac{\partial^2 h(\bar{P},\bar{T})}{\partial x \partial y} + \frac{3}{2(1+\nu)}\frac{\partial^2\tau_m}{\partial x \partial y} + \frac{1}{2}\nabla^2\tau_{xy} + \frac{1}{2}\left(\frac{\partial F_{b,y}}{\partial x} + \frac{\partial F_{b,x}}{\partial y}\right) = 0 \tag{17}$$

The other shear and normal stress tensor components are obtained in a similar manner as for the ones above.

Poroelastic media can deform when either the stress field or the pore pressure changes. Thus, rock properties, namely porosity and permeability depend on both the stress field and the pore pressure:

$$k = k(\boldsymbol{\tau}, P) \tag{18}$$

$$\phi = \phi(\boldsymbol{\tau}, P) \tag{19}$$

Correlations from the literature specify the above relations.

3. FINITE DIFFERENCE APPROXIMATION TO COUPLED FLUID AND HEAT FLOW

Our simulator's mass, energy, and momentum conservation equations are discretized in space using the integral finite difference method (Narasimhan and Witherspoon, 1976). In this method, the simulation domain is subdivided into Cartesian grid blocks and the conservation equations (Equation 1 for fluid components and energy, Equations 15-17 for momentum) are integrated over grid block volume, V_n, with flux terms expressed as an integral over grid block surface, Γ_n, using the divergence theorem:

$$\frac{d}{dt}\int_{V_n} M^k dV = \int_{\Gamma_n} \bar{F}^k \cdot \hat{n} d\Gamma + \int_{V_n} q^k dV \tag{20}$$

Volume integrals are replaced with volume averages:

$$\int_{V_n} M^k dV = M_n^k V_n \tag{21}$$

and surface integrals with discrete sums over surface averaged segments:

$$\int_{\Gamma_n} \bar{F}^k \cdot \hat{n} d\Gamma = \sum_m A_{nm} \bar{F}_{nm}^k \tag{22}$$

where subscript *n* denotes an averaged quantity over volume V_n, A_{nm} is the area of a surface segment common to volumes V_n and V_m, and double subscript *nm* denotes an averaged quantity over area A_{nm}. The definitions of the geometric parameters used in this discretization are shown in Figure 1.

Additional details of the finite difference approximation for these equations have been developed elsewhere (Pruess *et al.*, 1999; Winterfeld and Wu, 2018). Our simulator is massively parallel, with domain partitioning using the METIS and ParMETIS packages (Karypsis and Kumar, 1998; Karypsis and Kumar, 1999). Each processor computes Jacobian matrix elements for its own grid blocks, and exchange of information between processors uses MPI (Message Passing Interface) and allows calculation of Jacobian matrix elements associated with inter-block connections across domain partition boundaries. The Jacobian matrix is solved in parallel using an iterative linear solver from the Aztec package (Tuminaro et al., 1999).

4. MODELING DYNAMIC ADSORPTION IN TOUGH2-CSM

TOUGH2-CSM calculates fluid properties using TOUGH2 fluid property modules. We modified the EOS3 (Pruess, 1987) module to include additional aqueous components that can be used as tracers. These components have the same properties as water but can be tracked separately from it.

We then modified TOUGH2-CSM to include mathematical models of dynamic adsorption. Five options for this adsorption were added to TOUGH2-CSM: Henry's law, Langmuir equilibrium, Langmuir kinetic, two-site kinetic, and bilayer kinetic adsorption models (Kwok, 1995). The accumulation term in the TOUGH2-CSM mass conservation equations has the form:

$$\text{Accumulation term} = \frac{\partial\left(\phi \sum_p \rho_p S_p X_p^k\right)}{\partial t} \tag{23}$$

where subscript *p* refers to phase and subscript *k* refers to component. For the liquid phase (*p*=*l*), an additional expression is added to the accumulation term that represents the amount of adsorption per unit rock volume:

$$\text{Accumulation term} = \frac{\partial\left(\phi \sum_p \rho_p S_p x_{kp}\right)}{\partial t} + \delta_{lp} \frac{\partial\left((1-\phi)\Gamma_k\right)}{\partial t} \tag{24}$$

where Γ is the amount of adsorption per unit rock volume and δ is the kronecker delta.

The expression for Henry's law adsorption is linear:

$$\Gamma = \kappa c \tag{25}$$

where κ is the Henry's law slope. The concentration is given in mass per unit volume and is related to TOUGH2-CSM saturation and mass fraction by:

$$c = \rho S x \tag{26}$$

The expression for the Langmuir equilibrium model is the following:

$$\Gamma = \frac{Q_a K c}{1 + K c} \tag{27}$$

In the limit of zero concentration, the Langmuir equilibrium model reduces to Henry's law with a slope of $Q_a K$. In the limit of high concentration, the Langmuir equilibrium model approaches a constant concentration, Q_a.

The kinetic models have a time derivative of adsorption. The Langmuir kinetic model is the following:

$$\frac{d\Gamma}{dt} = k_a c (Q_a - \Gamma) - k_d \Gamma \tag{28}$$

where k_a end k_d are forward and reverse rate constants, respectively. At steady state, the Langmuir kinetic model reduces to the Langmuir equilibrium model with *K* given by k_a/k_d.

The two-site model is the following:

$$\frac{d\Gamma_1}{dt} = k_{a1} \check{c} (Q_{a1} - \Gamma_1) - k_{d1} \Gamma_1 \tag{29}$$

$$\frac{d\Gamma_2}{dt} = k_{a2} \check{c} (Q_{a2} - \Gamma_2) - k_{d2} \Gamma_2 \tag{30}$$

and consists of two Langmuir kinetic-type models for two independent adsorption sites. The concentration term, $\check{c}$, can be limited by the critical micelle concentration, C_{cmc}, when considering the adsorption of surfactant (Kwok, 1995):

$$\check{c} = \begin{bmatrix} c & c < C_{cmc} \\ C_{cmc} & c \geq C_{cmc} \end{bmatrix} \tag{31}$$

Finally, the bilayer model introduces dependence of site 2 adsorption on that of site 1:

$$\frac{d\Gamma_1}{dt} = k_{a1}\check{c}(Q_{a1} - \Gamma_1) - k_{d1}\Gamma_1 \tag{32}$$

$$\frac{d\Gamma_2}{dt} = k_{a2}\check{c}\left(Q_{a2}\frac{\Gamma_1}{Q_{a1}} - \Gamma_2\right) - k_{d2}\Gamma_2 \tag{33}$$

5. MODELING DISCRETE FRACTURES IN TOUGH2-CSM

We also modified TOUGH2-CSM to include discrete fractures. We used the EDFM method, introduced by Lee et al. (2001) and further extended by Li and Lee (2008) and Moinfar et al. (2014) to model them. Our grid is Cartesian and each grid block consists of matrix volume and can contain fracture volume as well. The matrix volume is equal to the grid block volume. Fractures are approximated as rectangular regions that represent the fracture area, and an associated fracture aperture. A grid block contains fracture volume if a rectangular fracture area intersects the grid block. The intersection of a plane with a rectangular parallelepiped is a polygon with three to six sides, as shown in Figure 2, and the fracture volume contributed to this grid block is that area of intersection multiplied by the fracture aperture. Multiple fractures can intersect a grid block and the grid block fracture volume is the sum of the contributions from each individual fracture:

$$V_{fr} = \sum_f A_f w_f \tag{34}$$

where subscript *f* refers to the discrete fractures, V_{fr} is the grid block fracture volume, A is area of intersection between the fracture and the grid block, and w is fracture aperture.

Each grid block has up to six neighbors. The fracture volume of one grid block communicates with that of another if the grid blocks are neighbors in the Cartesian grid and fracture volume in both have contributions from the same fracture, as shown in Figure 3a.

Fluid flows by Darcy flow between the fractures in the pair of neighboring grid blocks shown in Figure 3a. The transmissibility for this flow is the cross sectional flow area, given by the fracture aperture times the edge length of the polygon resulting from the intersection of the fracture plane with the grid block, divided by the distance between the centroids of the neighboring polygons:

$$T_{f12} = \frac{L_{12}w_f}{S_1+S_2} \tag{35}$$

where T_{f12} is the fracture-fracture transmissibility, and as illustrated in Figure 3b, S_1 is the distance from the centroid of the polygon on the left to the polygon edge, S_2 is the distance from the centroid of the polygon on the right to the polygon edge, and L_{12} is the edge length of the polygon resulting from the intersection of the fracture plane with the grid block.

Fluid also flows by Darcy flow between the fracture and the matrix. The cross sectional flow area for the transmissibility is the total face area of the fracture associated with a grid block and the distances for the transmissibility are half the fracture aperture and the average distance from a point in the grid block to the fracture plane, d_{avg}. The latter distance is obtained numerically by subdividing each grid block into a fine Cartesian grid and averaging the distance from each subdivision to the fracture plane, as illustrated in Figure 4:

$$d_{avg} = \frac{\sum_i V_i d_i}{\sum_i V_i} \tag{36}$$

where d_i is the distance from the subdivision to the fracture plane and V_i is the subdivision volume. The fracture-matrix transmissibility, T_{mf}, is then:

$$T_{mf} = \frac{2A_f}{\frac{w_f}{2}+d_{avg}} \tag{37}$$

Each matrix grid block and each fracture volume associated with a matrix grid block have a set of primary variables associated with them. The simulation thus consists of a mixture grid blocks that are single porosity (those containing only matrix) and double porosity (those containing matrix and fracture).

6. EXAMPLE SIMULATIONS

6.1 Tracer Simulations

Our first set of example problems were concerned with validating our conservative tracer transport formulations and were from Shook and Suzuki (2017), who analyzed a tracer test to estimate the fracture pore volume swept and the flow geometry. They used TOUGH2

to simulate a single well pair completed in a single vertical fracture set in non-fractured native rock. The half-length of the fracture is 99 m with a height of 75 m and an aperture of 0.02 m. The matrix width is 642.66 m to ensure semi-infinite behavior over the time scale of interest. The wells are completed only in the fracture, as shown in Figure 5.

In this case, the fracture is additionally assumed to span both damage zones in Figure 5 with permeability of 10^{-11} m^2. The initial temperature is 200 °C, and the initial pressure is 9800 kPa. Water at 25 °C is injected for one hour, followed with 25 °C water with 10% tracer by weight for one hour, and then with 25 °C water without tracer for the balance of the simulation. All injection and production rates are 2 kg/s.

Figure 6 shows a comparison of tracer histories between TOUGH2-CSM and Shook and Suzuki (2017). The shapes of the curves match. The TOUGH2-CSM data is reported as a mass fraction rather than a concentration as in the paper. Figure 7 is a comparison of temperature histories, and they match as well.

The above simulation assumed the damage zones in Figure 4 had the same permeability as the fracture. An additional case was run with Damage Zone 1 and 2 permeabilities of $4\cdot10^{-12}$ m^2 and $2\cdot10^{-12}$ m^2, respectively. Figure 8 shows a comparison of tracer histories between TOUGH2-CSM and Shook and Suzuki (2017), and the shapes of the curves match as well.

We next ran a number of simulations, from Kwok et al. (1995), to validate our mathematical models of dynamic adsorption. The simulation domain was a cylindrical annulus 88.4 mm in outer diameter, 3.5 mm inner diameter, and 35 mm in height. From a Henry's law slope of 0.198 and a retardation factor of 1.626, which were given, we obtained a porosity of 0.2403. Permeability was arbitrarily set at 10^{-12} m^2.

The two-dimensional rz simulation grid was 200×2. Axial thicknesses were equal and radial thickness was 10^{-5} m at the inner boundary and increased by a constant factor when traversed radially outward. Gravity was neglected, there was a single aqueous phase present, and there were three components, water, tracer and surfactant. Fluid was injected uniformly along the z-direction at a rate of 20 ml/hr. Three volumes, each equal to the simulation domain pore volume, of tracer and surfactant were injected first, followed by four such volumes of water. Only the surfactant component adsorbed on the rock. A comparison of effluent concentration profiles of tracer and surfactant, obtained at the outer system boundary and normalized by their injected concentrations, versus pore volume are shown for the cases described below. In general, agreement between the TOUGH2-CSM profiles and those from the simulations done in the reference are good.

Our first case used the Langmuir kinetic model with Q_a of 0.17551 kg/m^3, k_a of 8.7379 m^3/kg-s, and k_d of 10^{-1} s^{-1}. Injected tracer mass fraction was 0.0002 and that for surfactant was 0.0091. Figure 9 shows the comparison of results.

Our second case used the two-site model with Q_{a1} of 0.30886 kg/m^3, Q_{a2} of 0.86217 kg/m^3, k_{a1} of 1.4230 m^3/kg-s, k_{a2} of $3.24180\cdot10^{-5}$ m^3/kg-s, k_{d1} of $2.7140\cdot10^{-8}$ s^{-1}, and k_{d2} of $8.2000\cdot10^{-5}$ s^{-1}. Injected tracer mass fraction was 0.0002 and that for surfactant was 0.0019. Figure 10 shows the comparison of results.

Our third case used the bilayer model with Q_{a1} of 0.32861 kg/m^3, Q_{a2} of 0.84243 kg/m^3, k_{a1} of $1.6069\cdot10^{-3}$ m^3/kg-s, k_{a2} of $6.28366\cdot10^{-5}$ m^3/kg-s, k_{d1} of 0 s^{-1}, k_{d2} of $1.0763\cdot10^{-4}$ s^{-1}, and critical micelle concentration was 1.0 kg/m^3. Injected tracer mass fraction was 0.0002 and that for surfactant was 0.0019. Figure 11 shows the comparison of results.

6.2 Discrete Fracture Simulation

We ran a simulation to demonstrate the performance of our discrete fracture model. Our primary grid was 100×100×1 with each grid block a 1×1×5 m cube. We then added 115 discrete fractures to the primary grid. These rectangular fractures were input by specifying the location of a vertex along with two orthogonal vectors originating at that vertex that determine the rectangular fracture's geometry. One of those vectors was always along the z-direction (the fractures were vertical) and spanned the grid height. The other vector length, in the xy-plane, had a randomly selected orientation and length. The aperture of the fractures was 10^{-3} m. Figure 12 shows the primary grid and identifies the grid blocks containing these fractures.

The matrix permeability was $2\cdot10^{-19}$ m^2 and the fracture permeability was 10^{-11} m^2. There were two components, water and tracer, that had identical properties. The system was initialized with a single aqueous phase containing only water. Tracer was injected at $4.5\cdot10^{-4}$ kg/sec on the left of Figure 12 at the grid block shown by the arrow and produced at the right of Figure 13 at the grid blocks shown by the arrows, which were at constant pressure. The movement of tracer through the system is shown in Figures 13a-d. Tracer preferentially moves along the path of least resistance and does not enter dead ends in the fracture network and isolated fractures. Tracer also does not enter the matrix in significant amounts due to its low permeability.

6.3 EGS Collab Experiment 1 Simulations

We simulated tracer transport for the first EGS Collab SIGMA-V experiment. Figure 14 is a schematic, obtained from Leapfrog, of the region where this experiment was conducted. It shows the drift, the wells, and the hydraulically induced fracture that intersects two natural fractures. The region was simulated as a 49 m thick by 61m squared area with grid blocks of 1 m cubed. The fractures were all vertical with the hydraulic fracture approximated as a planar rectangle 18 m in height and 21 m in length, one of the natural fractures approximated as a planar rectangle 31 m in height and 41 m in length, and the other approximated as a planar rectangle 31 m in height and 48 m in length. The fracture apertures were all 0.0001 m. The intersections of these rectangles with the reservoir grid determine the grid blocks that contain both fracture and matrix. Figure 15 shows a xy-cross section of the grid with grid blocks that contain matrix

and fracture in red and those that contain only matrix in blue. The areal position of the wells are also shown, along with the layer they appear in.

The matrix porosity was 0.003 and there was a constant pressure boundary on all four lateral sides of the simulation domain. The initial pressure at the top layer was 6895 kPa. As shown in Figure 15, there was an injector well, E1-I, located at primary grid x-, y- and z-direction indices of (30,31,26). There are five producers, E1-PI, E1-PB, E1-OT, E1-PDT, and E1-PST, located at (40,30,24), (40,31,24), (35,31,20), (36,35,18), and (43,26,18), respectively. Tracer solution was injected at $2.91 \cdot 10^{-4}$ kg/sec for the first 360 seconds, along with $6.667 \cdot 10^{-3}$ kg/sec of water for the duration of the simulation. The producers were at constant initial pressure, which was in hydrostatic equilibrium. Figure 16 compares the simulated tracer concentration at the producers with experimental data obtained on November 8, 2018. The tracer concentrations of the experiment and simulation are in different units but their shapes are similar and the peaks occur at roughly the same time with the well E1-OT peak about three times that of well E1-PB. The match was obtained by adjusting the fracture and matrix permeabilities. The matrix permeability was $8 \cdot 10^{-16}$ m^2. The fracture permeability for layers 1-22 was $2.333 \cdot 10^{-10}$ m^2, that for layers 23-49 was $1.333 \cdot 10^{-10}$ m^2, and that in the vicinity of well E1-PB was $0.333 \cdot 10^{-10}$ m^2.

For the same fracture geometry, rock properties, and sources/sinks described above, thermal breakthrough simulations were conducted after matching the tracer response. The undisturbed rock temperature field, derived by the EGS-Collab Team based on borehole temperature measurements and heat transfer simulations, is set as the initial temperature distribution. With water injected at 15°C, the production temperature at E1-OT is shown in Figure 17 for 5 different injection flow rates. As expected, higher injection flow rates result in earlier breakthrough. With respect to the tracer response times, thermal breakthrough times are significantly longer.

7. SUMMARY AND CONCLUSIONS

We modified our TOUGH2-CSM simulator in order to simulate sorbing tracers and embedded fractures for the EGS Collab SIGMA-V project. We accomplished the former by modifying one of the simulator physical property modules to handle tracers, considered as additional components that reside in the water phase and have the same properties as water. We then added five options for tracer adsorption: Henry's law, Langmuir equilibrium, Langmuir kinetic, two-site kinetic, and bilayer kinetic adsorption. We modeled embedded discrete fractures as planar rectangles with an associated aperture. Flow through the reservoir matrix and those fracture representations was simulated using a reservoir grid that contains grid blocks that contain either matrix or matrix and fracture.

We verified our modifications by running tracer transport and adsorption problems from the literature, demonstrated our embedded discrete fracture model by a sample problem, and applied the embedded discrete fracture model to the first EGS-Collab SIGMA-V experiment where we matched experimentally obtained tracer production data in a reservoir containing a hydraulic fracture that intersects two natural fractures and simulated thermal breakthrough. Due to the success of this simulator modification, we will apply it to additional EGS-Collab SIGMA-V experiments and continue its modification in other areas of interest to the EGS-Collab SIGMA-V project.

8. ACKNOWLEDGEMENTS

This work was supported by Energi Simulation. This material was based upon work supported by the U.S. Department of Energy, Office of Energy Efficiency and Renewable Energy (EERE), Office of Technology Development, Geothermal Technologies Office, under Award Number DE-AC52-07NA27344 with LLNL, Award Number DE-AC05-76RL01830 with PNNL, and Award Number DE-AC02-05CH11231 with LBNL. Publication releases for this manuscript are under LLNL-CONF-744968 and PNNL-SA-131601. The United States Government retains, and the publisher, by accepting the article for publication, acknowledges that the United States Government retains a non-exclusive, paid-up, irrevocable, world-wide license to publish or reproduce the published form of this manuscript, or allow others to do so, for United States Government purposes. The research supporting this work took place in whole or in part at the Sanford Underground Research Facility in Lead, South Dakota. The assistance of the Sanford Underground Research Facility and its personnel in providing physical access and general logistical and technical support is acknowledged. The earth model output of the fractures was generated using Leapfrog Software. Copyright © Seequent Limited. Leapfrog and all other Seequent Limited product or service names are registered trademarks or trademarks of Seequent Limited.

REFERENCES

Karypis, G., Kumar, V., 1998. A parallel algorithm for multilevel graph partitioning and sparse matrix ordering. *Journal of Parallel and Distributed Computing* 48, 71-85.

Karypis, G., Kumar, V., 1999. A fast and high quality multilevel scheme for partitioning irregular graphs. *Siam J. Sci. Comput*. 20 (1), 359-392.

Kwok, W., Hayes, R.E., Nasr-El-Din, H.A., 1995. Modelling dynamic adsorption of an anionic surfactant on Berea sandstone with radial flow. *Chem. Eng. Sci.* 50, 769–783.

Lee, S. H., Lough M. F., and Jensen C. L., 2001. Hierarchical modeling of flow in naturally fractured formations with multiple length scales. *Water Resources Research* 37 (3):443–55.

Li, L. and Lee, S. H., 2008. Efficient field-scale simulation of black oil in a naturally fractured reservoir through discrete fracture networks and homogenized media. *SPE Reservoir Evaluation and Engineering* 11 (04):750–58.

Moinfar, A., Varavei, A., Sepehrnoori, K., and Johns, R. T., 2014. Development of an efficient embedded discrete fracture model for 3D compositional reservoir simulation in fractured reservoirs. *SPE Journal* 19 (02):289–303.

Narashimhan, T. N. & Witherspoon, P. A.: An integrated finite difference method for analysis of fluid flow in porous media. *Water Resources Res.* 12 (1976), pp. 57–64.

Pruess, K. 1987. TOUGH User's Guide. Report LBNL-20700, Lawrence Berkeley National Laboratory, Berkeley, California.

Pruess, K., Oldenburg, C., and Moridis G. 1999. TOUGH2 User's Guide, Version 2.0. Report LBNL-43134, Lawrence Berkeley National Laboratory, Berkeley, California.

Shook, G. Michael and Suzuki, A. Use of tracers and temperature to estimate fracture surface area for EGS reservoirs. *Geothermics* 67 (2017): 40-47.

Tuminaro, R.S., Heroux, M., Hutchinson, S.A., Shadid, J.N., 1999. Official Aztec user's guide version 2.1. Massively Parallel Computing Research Laboratory, Sandia National Laboratories, Albuquerque, NM.

Winterfeld, P. H. and Wu, Y.-S. 2014. Simulation of CO_2 Sequestration in Brine Aquifers with Geomechanical Coupling. In *Computational Models for CO_2 Sequestration and Compressed Air Energy Storage,* edited by J. Bundschuh and R. Al-Khoury, Chapter 8, pp. 275-303, New York, NY: CRC Press.

Winterfeld, P. H. and Wu Y.-S., 2015. Simulation of Coupled Thermal-Hydrological-Mechanical Phenomena in Porous Media, *SPE Journal*, December 2016, p. 1041-1049.

Winterfeld, P. H. and Wu Y.-S., 2018. Simulation of Coupled Thermal-Hydrological-Mechanical Phenomena in Heterogeneous and Radial Systems, presented at TOUGH Symposium 2018, Berkeley, CA, October 8-10.

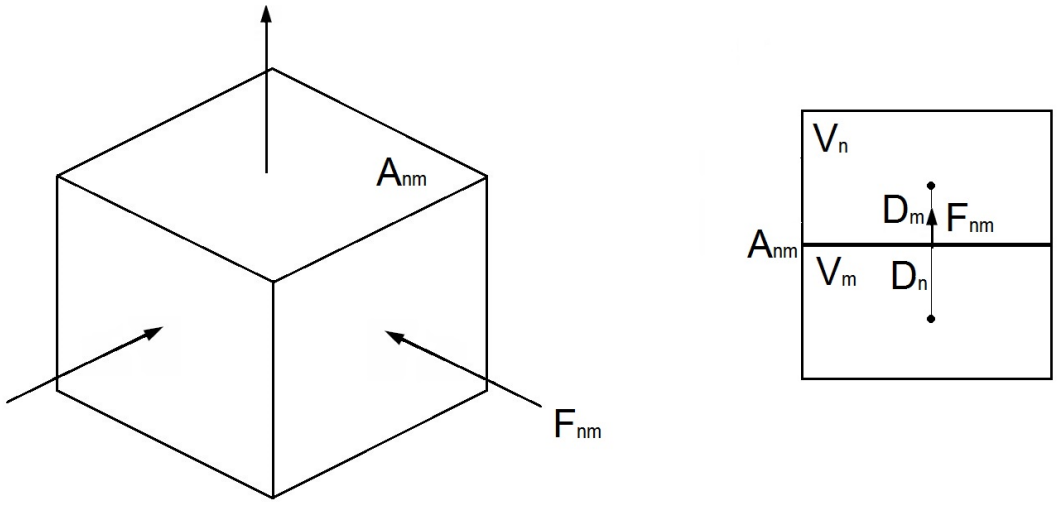

Figure 1. Parameter definitions for the integral finite difference method. The figure on the right shows two neighboring grid blocks and the interface between them.

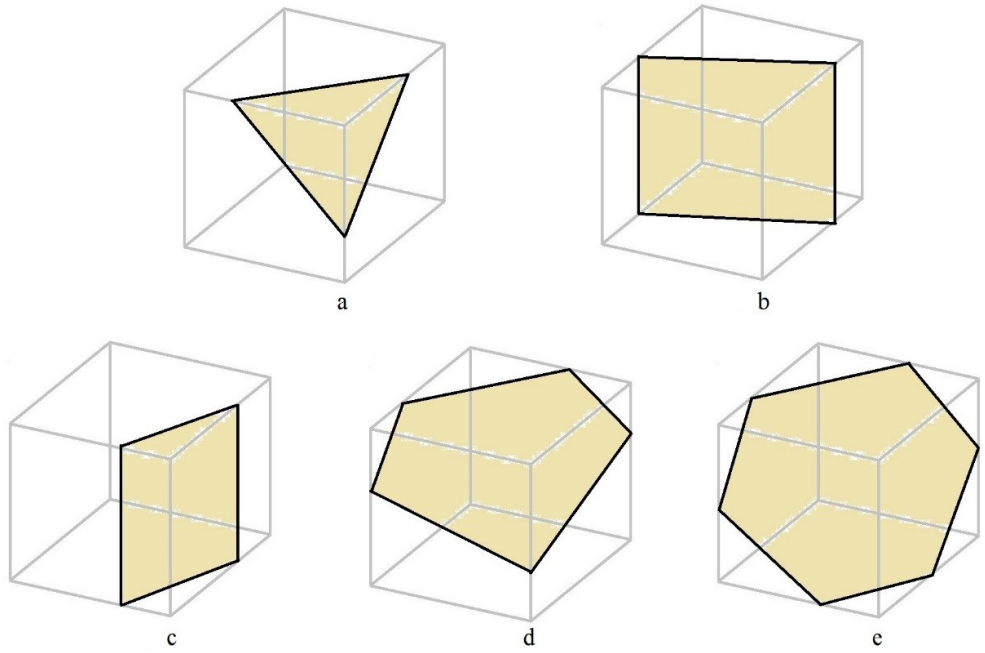

Figure 2. Intersections of a plane with a rectangular parallelepiped: triangle (a), quadrilateral (b,c), pentagon (d), hexagon (e).

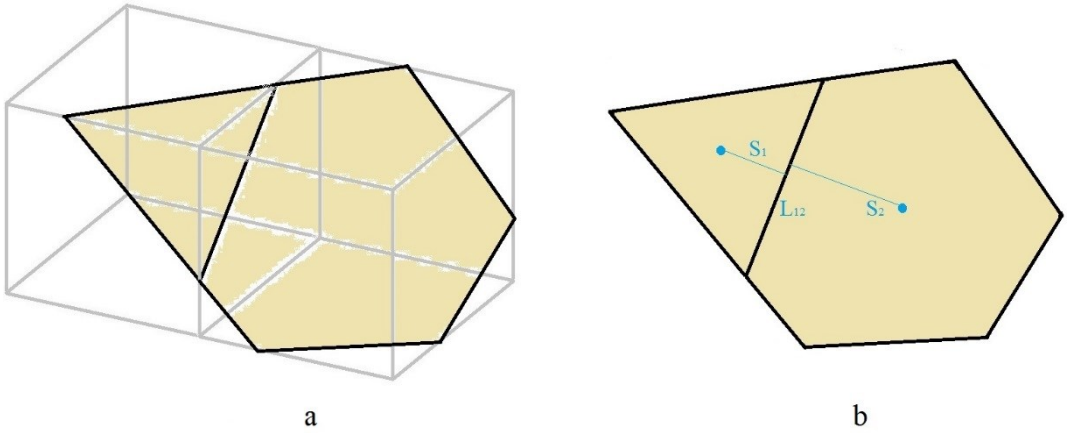

Figure 3. Two neighboring grid blocks each with fracture volume, in tan, contributed from the same fracture (a); parameters used to calculate flow transmissibility for flow between the two fracture volumes (b).

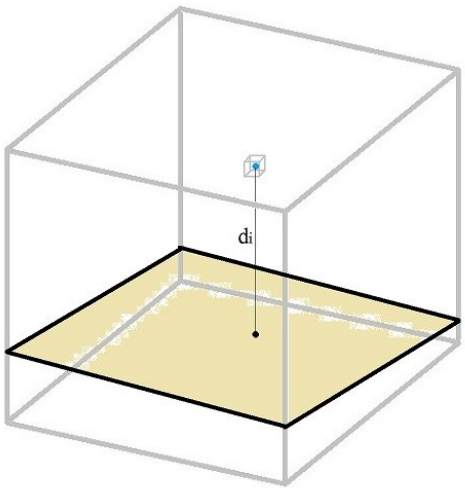

Figure 4. Grid block subdivision, shown as small cube, and distance d_i from subdivision to fracture plane for calculation of average distance from a point in the grid block to the fracture plane.

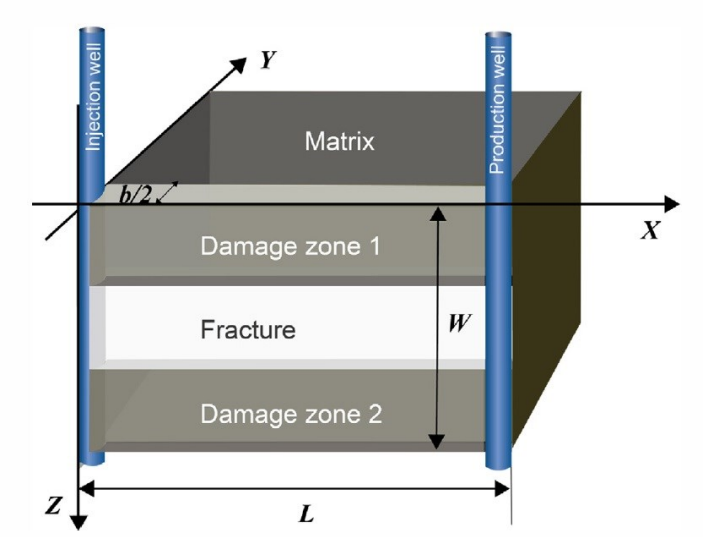

Figure 5: Schematic of the EGS reservoir used in the comparison, from Shook and Suzuki (2017).

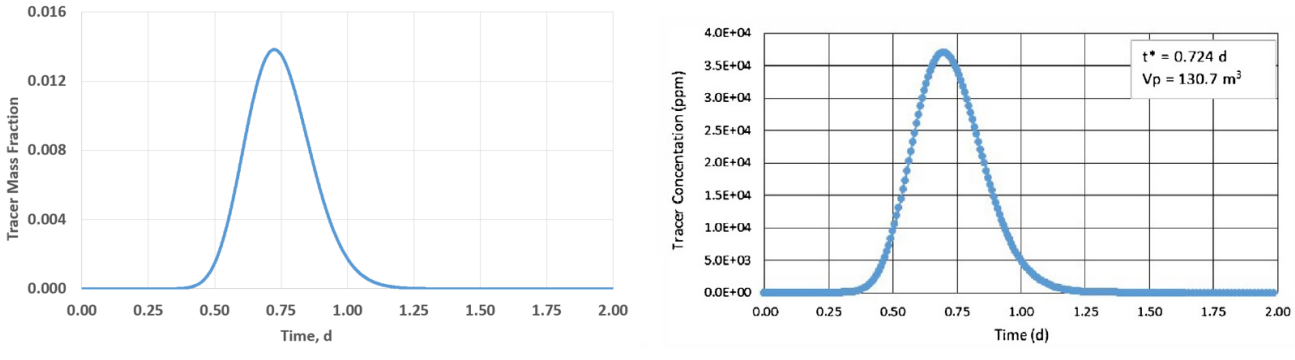

Figure 6. Comparison of tracer concentration/mass fraction profiles between TOUGH2-CSM (left) and Shook and Suzuki (2017) (right).

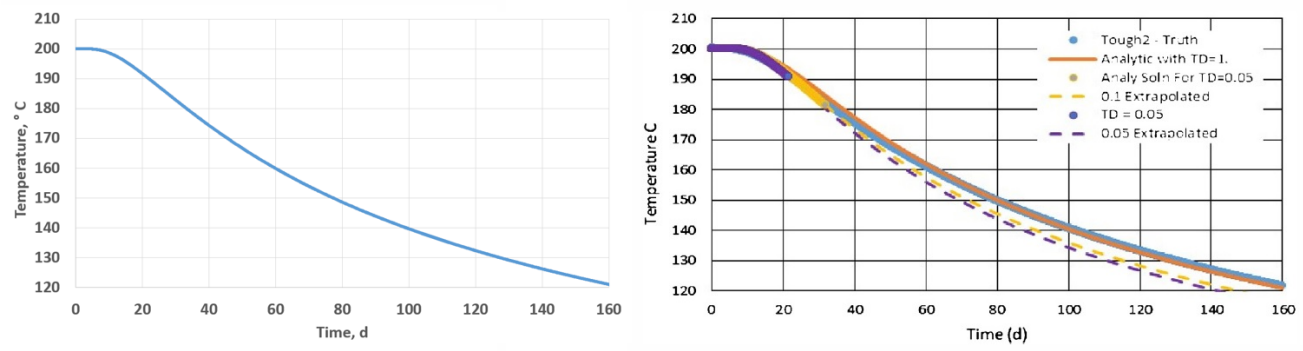

Figure 7. Comparison of temperature profiles between TOUGH2-CSM (left) and Shook and Suzuki (2017) (right).

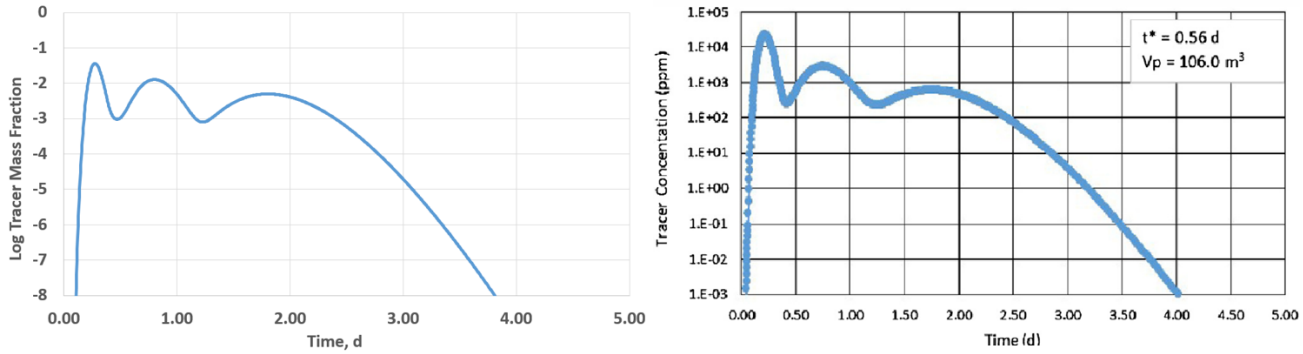

Figure 8. Comparison of tracer concentration/mass fraction profiles between TOUGH2-CSM (left) and Shook and Suzuki (2017) (right) for nonzero damage zone permeability.

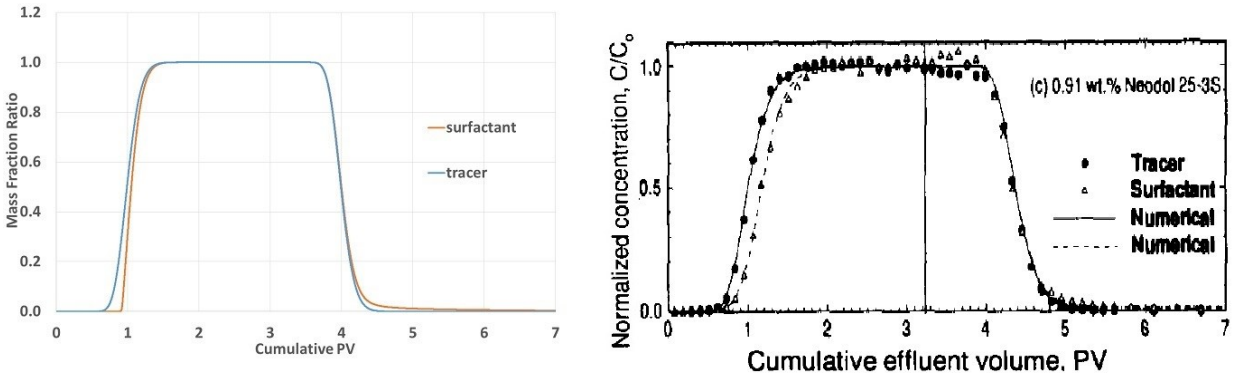

Figure 9. Comparison of TOUGH2-CSM simulation (left) with that from Kwok et al. (1995) (right) for Langmuir kinetic adsorption model.

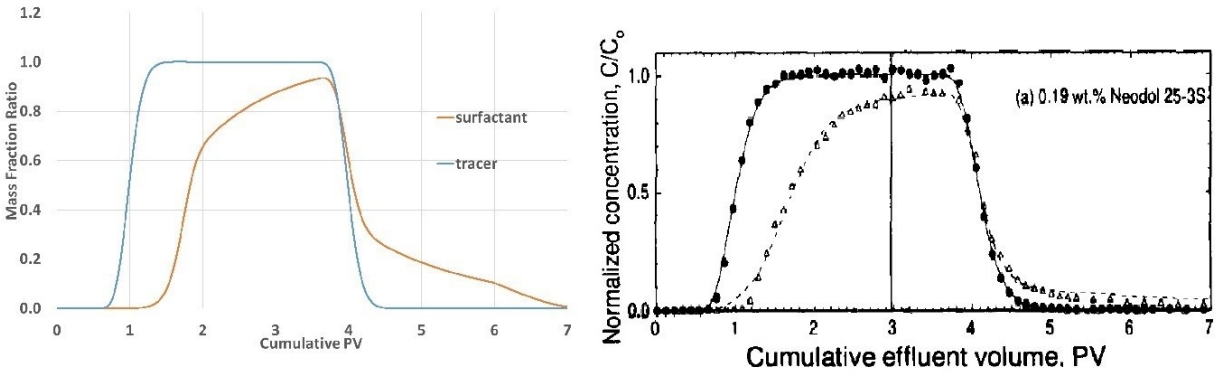

Figure 10. Comparison of TOUGH2-CSM simulation (left) with that from Kwok et al. (1995) (right) for two-site adsorption model.

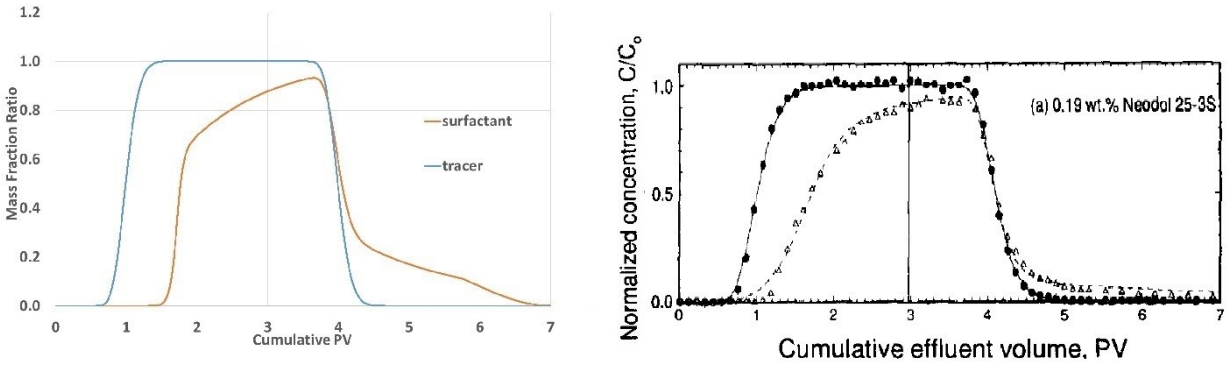

Figure 11. Comparison of TOUGH2-CSM simulation (left) with that from Kwok et al. (1995) (right) for bilayer adsorption model.

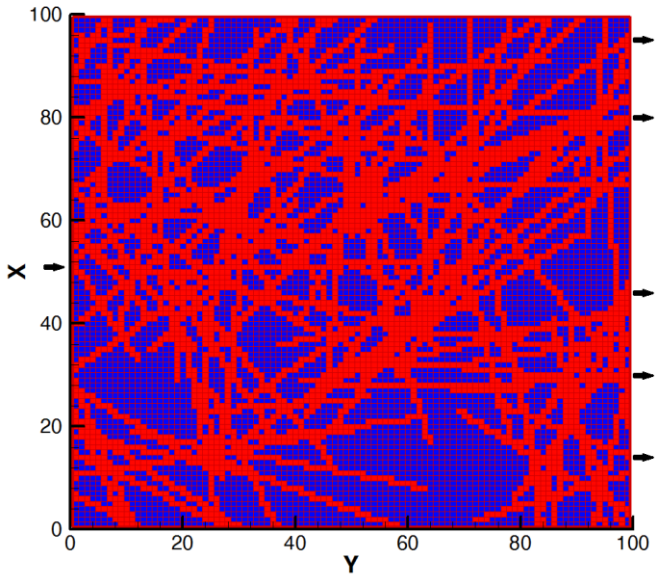

Figure 12. Cross section of the grid showing grid blocks containing fractures in red and those without fractures in blue. Injection occurs at the left arrow and production at the right ones.

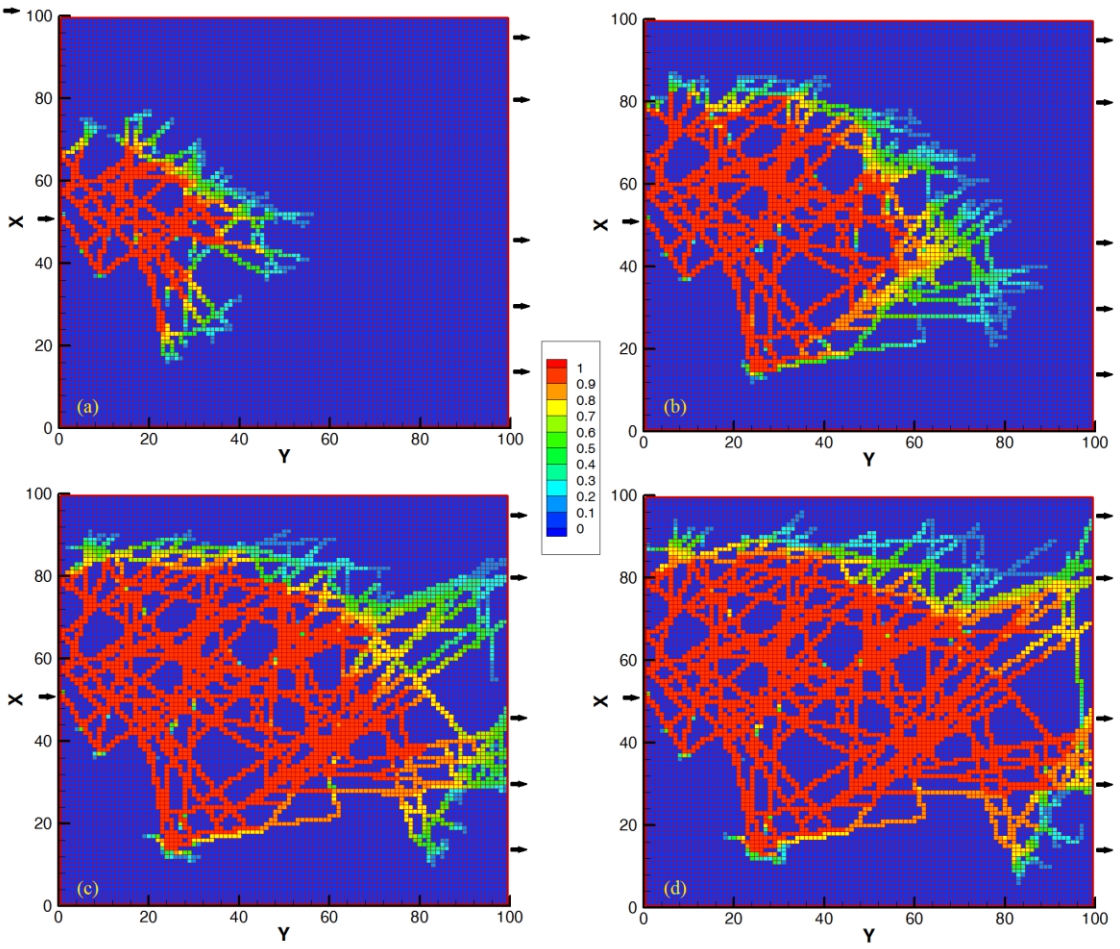

Figure 13. Cross section of grid showing movement of tracer, shown as mass fraction, through the fracture network: a) $2 \cdot 10^6$ seconds, b) $5 \cdot 10^6$ seconds, c) $8 \cdot 10^6$ seconds, d) 10^7 seconds.

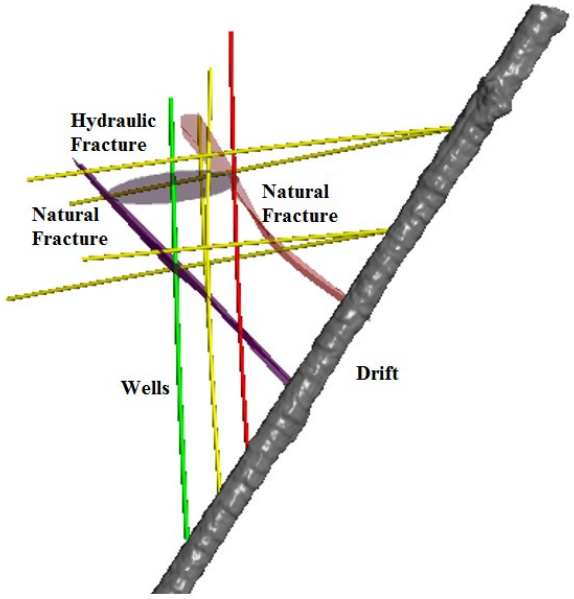

Figure 14. Schematic of region where first EGS Collab SIGMA-V experiment is being conducted, showing drift, wells, and fractures.

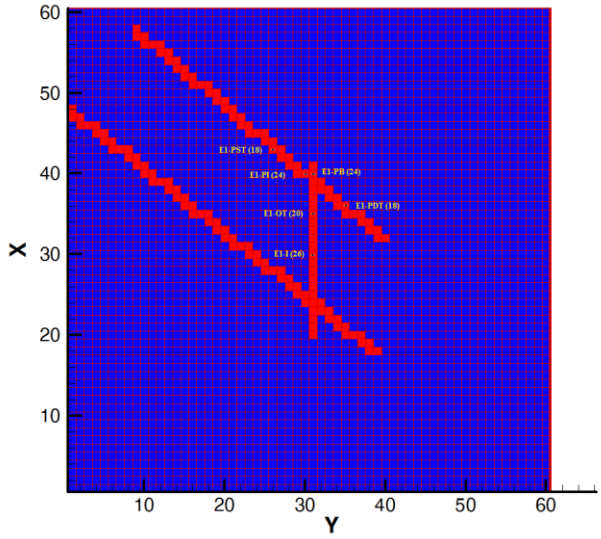

Figure 15. Cross section of grid showing grid blocks that contain matrix and fracture in red and those that contain only matrix in blue. The vertically oriented region is the hydraulic fracture and the parallel ones are the natural fractures. The well areal location is shown by the dots with the well layer in parentheses.

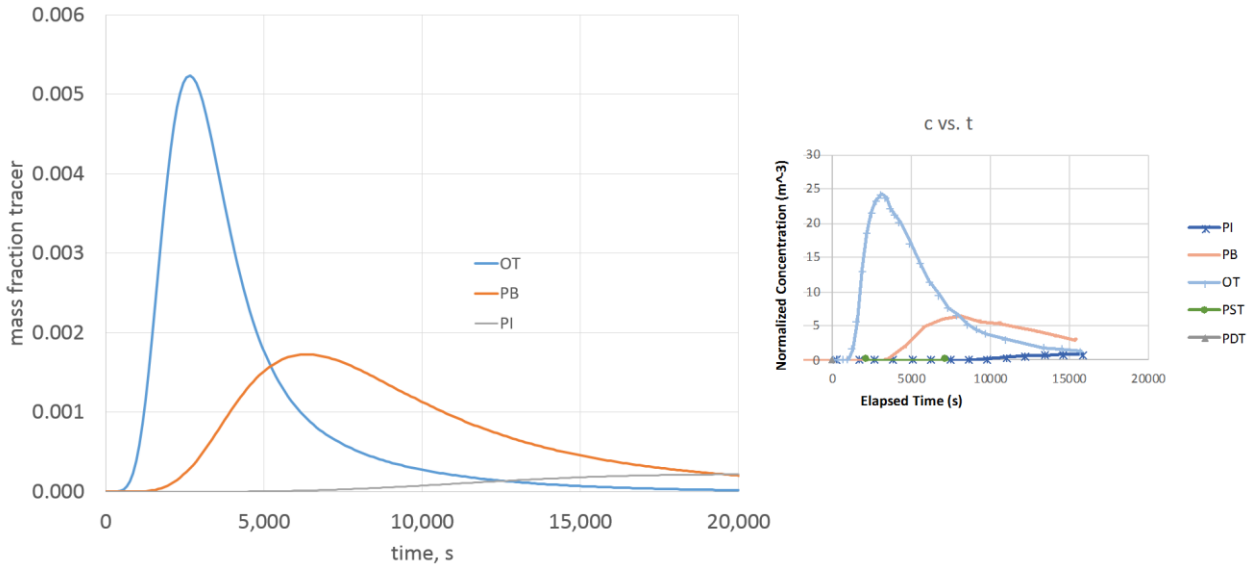

Figure 16. Comparison of simulated producer tracer concentration, left, to experimental data from November 8, 2018, right.

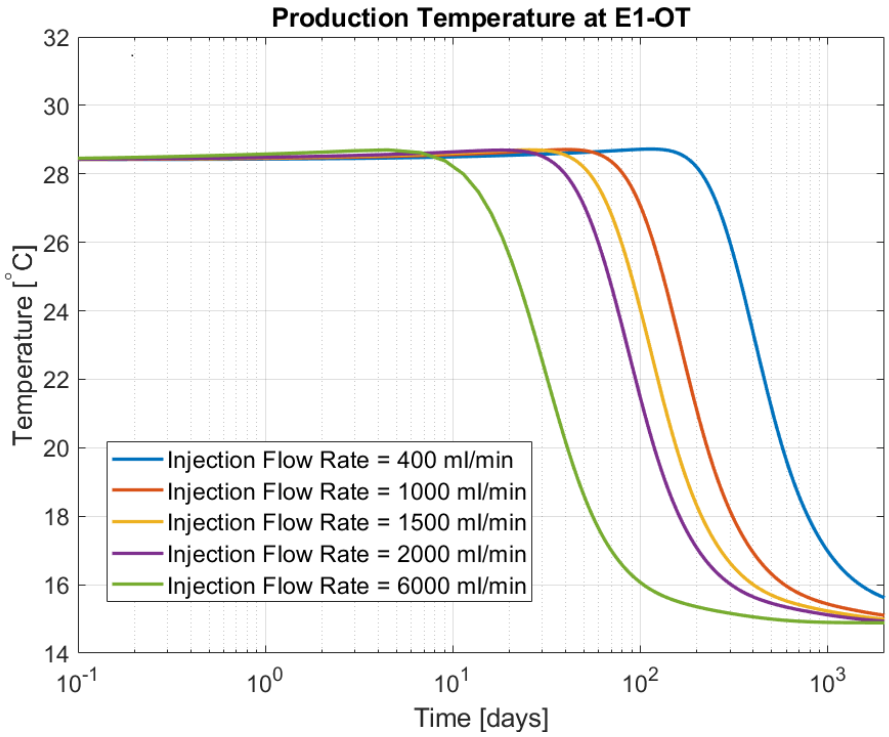

Figure 17. Thermal breakthrough simulations for various injection rates for above case.